RSC Advances

PAPER

View Article Online
View Journal | View Issue

Cite this: *RSC Adv.*, 2020, **10**, 30519

Electrocatalytic reduction of oxygen at platinum nanoparticles dispersed on electrochemically reduced graphene oxide/PEDOT:PSS composites†

Teklewold Getachew,*[a] Fitsum Addis,[a] Solomon Mehretie,[a] Hin-Lap Yip,[b] Ruidong Xia[b] and Shimelis Admassie[ab]

Composites of commercially available graphene oxide (GO) and poly(3,4-ethylenedioxythiophene):poly(styrenesulfonate) (PEDOT:PSS) with solvent additive ethylene glycol (EG) were investigated as an alternative support for Pt nanoparticles towards the electrocatalytic reduction of oxygen. The surface characteristics of the materials were examined using atomic force microscopy (AFM), X-ray diffraction (XRD), field-emission scanning electron microscopy (FESEM), and energy dispersive X-ray spectroscopy (EDS). Cyclic voltammetry (CV) and linear sweep voltammetry (LSV) at rotating disk electrodes (RDEs) and rotating ring-disk electrodes (RRDEs) were used to characterise the electrocatalytic activities of the composites materials. The structural and electrochemical studies reveal that the addition of EG favours the homogeneous distribution of Pt particles with reduced particle size and improves the electrocatalytic properties. A 30% and 16% increase in electrochemically active surface area (ECSA), a 1.2 and 1.1 fold increase in specific area activity (SA), and a 1.5 and 1.2 fold increase in mass activity (MA) were observed for 30% and 40% Pt loading on PEDOT:PSS after the addition of EG. A composite of rGO and PEDOT:PSS(EG) was investigated for different (w/w) ratios of PEDOT:PSS and rGO. The 1 : 2 w/w ratio showed an enhanced catalytic activity with high limiting current, more positive onset potential, higher SA and MA with lower H_2O_2 yield compared to PEDOT:PSS(EG) and rGO and previously reported values for PEDOT:PSS.

Received 14th June 2020
Accepted 13th August 2020

DOI: 10.1039/d0ra05232a

rsc.li/rsc-advances

Introduction

Commercialization and widespread application of fuel cells and metal–air batteries in different sectors require the development of catalyst materials with low cost and satisfactory activity and stability.[1,2] In all these applications, the oxygen reduction reaction (ORR) at the cathode is the major contributor to single-cell efficiency losses due to its slow kinetics. Hence, platinum (Pt) and Pt-based alloys are commonly employed catalysts to improve the kinetics of the ORR.[2,3] However, the cost of Pt is very high and its supply is limited.[4] To circumvent this problem, several authors investigated and reported non-Pt based catalysts,[5,6] while others used Pt-dispersed nanoparticles on different supports[1,2] to reduce the amount of Pt-loading. The dispersion of Pt on catalyst supports not only reduces the cost of the noble metals but also improves the efficiency of the electrocatalysts.[7,8] Higher catalytic activity on a support matrix requires nanometric dimensions with a uniform distribution of Pt particles.[9] Hence, an ideal Pt catalyst support material needs to have several properties including high surface area, good electronic conductivity and electrochemical stability, strong cohesion to catalyst particles and the ability to homogeneously distribute uniformly sized nanoparticles.[10,11]

Various carbon-based materials such as carbon blacks, carbon nanotubes, carbon nanofibers, multiwall carbon nanotubes, conducting polymers and graphene have been extensively investigated as Pt supports for ORR.[1,8,9,12–14] Among these, graphene (or reduced graphene oxide, rGO) has become more attractive in recent years due to its unique physicochemical properties, like excellent conductivity, high charge-carrier mobility, good transparency, great mechanical flexibility, and huge specific surface area (theoretically 2630 $m^2\ g^{-1}$ for a single layer).[10,13–15] However, weak interaction of graphene with metals and restacking of graphene sheets due to pi–pi interaction are still some of the problems that are hindering its application as electrocatalyst support for Pt nanoparticles.[11,14] On the other hand, conducting polymers, which are good catalysts for ORR and support materials for the dispersion of Pt metal catalysts, prevent aggregation of graphene sheets and particle

[a]*Department of Chemistry, Addis Ababa University, PBox 1176, Addis Ababa, Ethiopia. E-mail: teklewold.getachew@aau.edu.et*

[b]*State Key Laboratory of Luminescent Materials and Devices, Institute of Polymer Optoelectronic Materials and Devices, School of Materials Science and Engineering, South China University of Technology, 381 Wushan Road, Guangzhou, 510640, PR China*

† Electronic supplementary information (ESI) available. See DOI: 10.1039/d0ra05232a

agglomeration in addition to their high accessible surface area, low resistance and high stability in three-dimensional structure.[15–18]

Among conducting polymers, PEDOT:PSS is one of the most versatile and commercially available polymers successfully used in many different applications like organic solar cells, organic light emitting diodes, energy storage, transistors and sensors.[19] It can also be promising support material for Pt particle dispersion due to its chemical stability, dispersibility in water and some organic solvents, tunable conductivity and electrochemical performance.[20,21] Though, dependent on the method of synthesis and microstructures, PEDOT[22,23] and PEDOT:PSS[24] also shows electrocatalytic activity for ORR. Since the electrocatalytic ORR on Pt in acidic solution is a proton-coupled electron transfer reaction,[25] PEDOT:PSS, which has a polyanionic phase (PSS) will promote proton transport. The conducting polymer phase (PEDOT) further ensures electronic transport.[26] Moreover, the high boiling point polar organic compounds like ethylene glycol added into PEDOT:PSS aqueous solution to improve its conductivity[27] is known to improve the activity of Pt-supported catalyst by decreasing the average particle size, inhibition of growth of Pt particle, and evenly dispersion of Pt particle.[28] Hence, a composite of rGO and PEDOT:PSS treated with ethylene glycol combined the best features of each material. As part of numerous effort in the search for reducing the amount of Pt used in the electrocatalytic reduction of oxygen, herein, we report the potential application of commercially available GO and PEDOT:PSS composites with solvent additive EG as an alternative support for Pt nanoparticles towards ORR.

Experimental

Materials

Potassium nitrate (Riedel de Haen), potassium hexacyanoferrate(III) (Riedel de Haen), ethylene glycol (Sigma-Aldrich), sodium sulfate (Sigma-Aldrich), 5 wt% Nafion solution (Sigma-Aldrich), 4.0 mg mL^{-1} graphene oxide dispersion in water (Sigma-Aldrich), 70% perchloric acid (Fluka), 98% sulfuric acid (Carlo Erba Reagents), hexachloroplatinic acid (Research Lab Fine Chem Industries) and Clevios PH1000 (PEDOT:PSS) (Heraeus) were used for the preparation of electrolyte solutions and inks for the modified glassy carbon electrode (GCE). Nitrogen and oxygen gases were purchased in cylinders from Chora gas & chemical product factory (Addis Ababa). Deionized (DI) water was used throughout the experiment.

Preparation of the modified glassy GCE

The Pt support were first prepared by drop casting 3 μL of PEDOT:PSS without EG (PEDOT:PSS), PEDOT:PSS (PEDOT:PSS(EG)) and rGO/PEDOT PSS with EG (rGO/PEDOT PSS(EG)) onto a 0.196 cm^2 GCE (polished with 0.05 μm alumina powder). 6 vol% EG which is optimal concentration to improve the conductivity was added on PEDOT:PSS.[29] The addition of EG induces a conformational change in the PEDOT chain from a benzoid with a preferred coiled structure to a quinoid with a preferred linear or expanded-coil structure. This conformational change results in an increase in the intrachain and interchain charge-carrier mobility, so the conductivity is enhanced.[27] The films were then dried under room temperature overnight. The GO : PEDOT:PSS(EG) composites were prepared by mixing solution of GO and PEDOT:PSS(EG) in weight ratios of 2 : 1, 1 : 1, 1 : 2, 1 : 3 and 1 : 5 (GO : PEDOT:PSS(EG)). The electrochemical reduction of GO to rGO was carried out with CV in the potential range 0 to −1.5 V *vs.* Ag/AgCl at a scan rate of 50 mV s^{-1} in N_2 saturated 0.1 M Na_2SO_4 for 20 cycles. 30 Pt particles were then electrodeposited onto PEDOT:PSS, PEDOT:PSS(EG) and rGO/PEDOT:PSS(EG) potentiostatically from a 5 mM H_2PtCl_6 in 0.5 M H_2SO_4 by applying a potential of −0.15 V (*vs.* Ag/AgCl) until the amount of charge consumed to reduce Pt(IV) to Pt(0) were 10% (m_{Pt} = 3.6 μg), 20% (m_{Pt} = 8.1 μg), 30% (m_{Pt} = 13.85 μg) and 40% (m_{Pt} = 21.6 μg) of the total mass the catalytic material assuming 100% current efficiency.[31,32] The quantity of electricity associated with double-layer charging and the reduction of surface oxide is obtained by integration in the double layer region and subtracted from the total charge for determining the mass of platinum loading. 32 3 μL of Nafion (0.05%) dropped on the catalyst film as a binder.[33]

For comparison purposes, a thin-film electrode made from a commercial 20 wt% Pt/C catalyst (ETEK) were deposited on rotating glassy carbon electrode with Pt loading of 20 μg_{Pt} cm^{-2}. 10 mg of a 20 wt% Pt/C catalyst (ETEK), 1 mL of isopropanol, 3.98 mL of deionized water and 20 μL of 5 wt% Nafion ionomer solution were mixed, ultrasonicated for 60 minutes in a water bath for the catalytic ink formation. 10 μL of the resulting suspension was dropped on glassy carbon disc electrode (0.196 cm^2) dried using solvent evaporation by covering the catalyst ink-coated electrode with a beaker to get smooth and crack free film.[36]

Physical characterization

XRD spectra of the catalysts were collected using Rigaku Smart Lab SE X-ray diffractometer (Cu-Kα radiation at λ = 0.15406 nm). The average crystallite size of the nanoparticles was estimated using the Debye–Scherrer eqn (1):[28,34]

$$Z = \frac{k\lambda}{B_{2\theta}\cos\theta} \quad (1)$$

where Z is the diameter of the average crystallite size (angstrom or nm); λ is the X-ray wavelength (1.5406 A) for Cu Kα; θ is the Bragg angle; k is the Scherrer constant (typically from 0.9 to 1.0); B is the full width at half maximum.

AFM was used to study the sample's surface morphology and dispersion of Pt nanoparticles on PEDOT:PSS and PEDOT:PSS(EG) using a Nanotec Electronica SPM with and without the EG. The images were processed with WsxM software (v3.1).

The morphology of rGO/PEDOT:PSS(EG)/Pt was characterized by a FESEM (Hitachi, S-4800) and an EDS (HORIBA, EX-250) coupled on the FESEM was used to confirm the component of the rGO/PEDOT:PSS(EG)/Pt.

Electrochemical characterization

Electrodes and instrumentation. A potentiostat/galvanostat (Autolab PGSTAT 128N) connected to a computer with general purpose electrochemical system (GPES v 4.9) software is used to

characterize the electrochemical properties of the electrocatalysts using a rotating disk glassy carbon (RDGC) working electrode (0.196 cm^2). RRDE measurements were carried out at room temperature on a Pine bipotentiostat (model AFCBP1) connected to a computer with aftermath (v 1.2.5033) software. Glassy carbon disk electrode (0.2472 cm^2) surrounded by a Pt ring (0.1859 cm^2) was used for RRDE measurements. Silver/silver chloride (Ag/AgCl, 3 M KCl) and a platinum wire served as reference and counter electrodes, respectively. Pine rotation speed controller (AFMSRCE 2957) was used during the RDE and RRDE measurements. The measured potential of this reference electrode was converted to the RHE reference scale using E (*vs.* RHE) = E (*vs.* Ag/AgCl) + 0.21 V + 0.0591 V × pH.[35] Correction for IR drop was made after solution resistance were determined using electrochemical impedance spectra obtained for RDE catalyst layers using a frequency response analyzer (FRA, AutoLab) under N_2 or O_2 atmosphere (1600 rpm) in the frequency range from 10 kHz to 0.1 Hz with a 5 mV amplitude voltage perturbation.

Determination of electrochemical active surface area (ECSA). PEDOT:PSS/Pt, PEDOT:PSS(EG)/Pt and rGO/PEDOT:PSS(EG)/Pt electrode were cycled between 0 and 1.20 V *vs.* RHE for 40 cycles at 200 mV s^{-1} in 0.1 M $HClO_4$ nitrogen saturated (25 min) solution to remove residues hidden in the porous electrode and obtain stable CV curves. Then, cyclic voltammograms (3 cycles) recorded at a scan rate of 20 mV s^{-1} between 0.05 V and 1.20 V were used to determine the ECSA of the Pt catalysts. The ECSA was estimated using eqn (2) by integrating the hydrogen adsorption charge (Q) in the potential scan (0.40–0.075 V) after correction for double-layer charging.[28,36]

$$\mathrm{ECSA} = \frac{Q}{m \times 210} \tag{2}$$

where Q is the charges exchanged during hydrogen adsorption (μC); m is the mass of Pt loading (μg) and the numerical value 210 μC cm^{-2} represents the charge required to oxidize a monolayer of hydrogen on Pt surface.

Determination of kinetic current (i_k), mass activity (MA) and specific area activity (SA). After the ECSA measurements, linear sweep voltammograms on a RDE were recorded at 20 mV s^{-1} between 1.03 V and 0.05 V under O_2 or N_2 saturated 0.1 M $HClO_4$. The net faradaic current was obtained by subtracting the voltammogram recorded under N_2 from the one recorded under O_2.[36,37] Then, the mass transport corrected kinetic current is extracted from the mixed activation-diffusion region of linear sweep voltammograms using eqn (3):[38]

$$i_k = \frac{i_{lim} \times i}{i_{lim} - i} \tag{3}$$

where i is the measured current at a specified potential, i_{lim} is the measured limiting current, and i_k is the kinetic current. MA and SA were calculated using eqn (4) and (5).[36,39]

$$\mathrm{MA}\ \left(\mathrm{A\ mg^{-1}}\right) = \frac{i_k}{m_{Pt}} \tag{4}$$

$$\mathrm{SA}\ \left(\mathrm{mA\ cm^{-2}}\right) = \frac{i_k}{A_r} \tag{5}$$

where i_k is kinetic current, m_{Pt} mass of Pt and A_r real surface area.

Determination of collection efficiency (N), number of electrons transferred (n) and percentage of H_2O_2 (% H_2O_2). For the RRDE measurement, the disk and ring currents were recorded as a function of the disk potential scanned between 0 V and 1.2 V *vs.* RHE at 10 mV s^{-1} at one rotation speed (1600 rpm). The ring electrode potential being held at +1.3 V *vs.* RHE. N was determined using 1 M KNO_3 and 10 mM $K_3Fe(CN)_6$ (Fig. S1 and S2†) deaerated with pure nitrogen.[34,40] The equations used to calculate n, % H_2O_2 and N are the following:[40]

$$n = \frac{4i_d}{i_d + \frac{i_r}{N}} \tag{6}$$

$$\%\ \mathrm{H_2O_2} = \frac{200i_r}{i_d + \frac{i_r}{N}} \tag{7}$$

$$N = -\frac{i_r}{i_d} \tag{8}$$

where N is the collection efficiency of the rotating ring disk electrode (RRDE), and i_d and i_r are the disk and ring electrode currents, respectively.

Stability and electrochemical crossover test. The 3 M methanol (MeOH) tolerance ability of the catalyst was analyzed by chronoamperometry in O_2-saturated 0.1 M $HClO_4$ solution at a rotation speed of 1600 rpm and an applied potential of 0.8 V (*vs.* RHE). The durability was performed by chronoamperometry in O_2-saturated 0.1 M $HClO_4$ at a rotation speed of 1600 rpm and an applied potential of 0.8 V (*vs.* RHE) for 10 000 s.

Results and discussion

Surface characterization

The crystalline structure of Pt nanoparticles dispersed on to PEDOT:PSS/Pt(30%), PEDOT:PSS (EG)/Pt(30%) and rGO/PEDOT:PSS(EG)/Pt(30%) were investigated by XRD studies. Fig. 1 shows the XRD patterns of PEDOT:PSS/Pt(30%), PEDOT:PSS(EG)/Pt(30%) and rGO/PEDOT:PSS(EG)/Pt(30%) films. A broad peak (Fig. 1a) at 25° observed in all materials correspond to the (020) plane of PEDOT:PSS.[41] The peaks at 2θ = 39.9°, 46.5°, 67.7°, and 81.9° correspond to the diffraction planes (111), (200), (220), and (311) of Pt, respectively.[15]

The average crystallite size of PEDOT:PSS supported Pt was calculated from the broadening of the (111) diffraction peak using Debye–Scherrer eqn (1) and Fig. 1b. The average crystallite size of Pt obtained by using EG is 7.3 nm which is smaller compared to the deposition of Pt in the absence of EG (7.9 nm). But, the incorporation of rGO further increased the average crystallite size of Pt supported on rGO/PEDOT:PSS(EG) to 7.9 nm. The AFM images for PEDOT:PSS/Pt (Fig. 2b) and PEDOT:PSS(EG)/Pt (Fig. 2c) shows small cluster of particles not shown in PEDOT:PSS (Fig. 2a) confirming the deposition of Pt particle on PEDOT:PSS films. PEDOT:PSS(EG)/Pt (Fig. 2c) film shows small Pt nanoparticles and a full coverage of the Pt particle compared to PEDOT:PSS/Pt (Fig. 2b). The incorporation

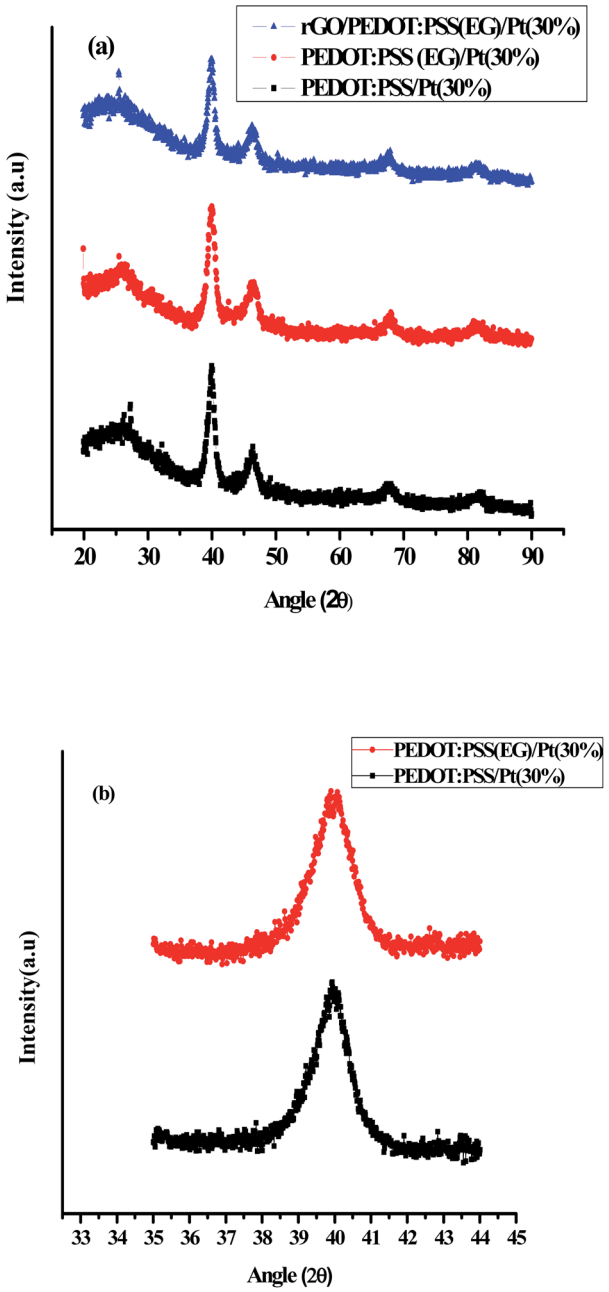

Fig. 1 XRD patterns of (a): PEDOT:PSS/Pt(30%), PEDOT:PSS(EG)/Pt(30%), and rGO/PEDOT:PSS(EG)/Pt(30%) (b): over a narrow range of 2θ (35–44 degrees) for PEDOT:PSS/Pt(30%) and PEDOT:PSS(EG)/Pt(30%).

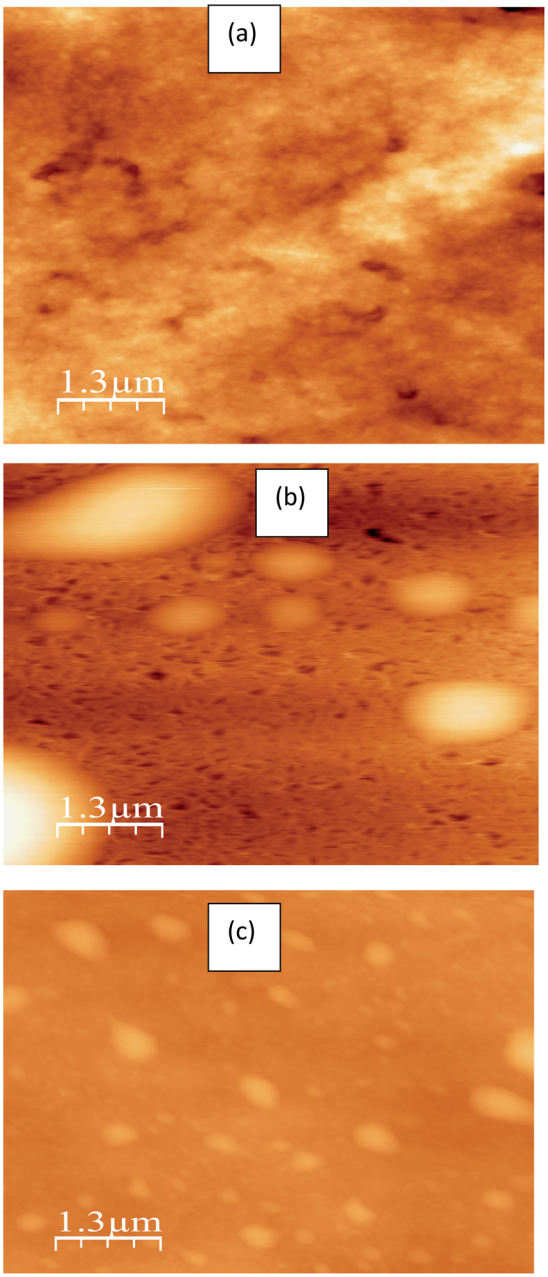

Fig. 2 The 2D AFM images of the: (a) PEDOT:PSS (b) PEDOT:PSS/Pt and (c) PEDOT:PSS (EG)/Pt.

of EG in PEDOT:PSS not only minimizes the rate of growth of Pt clusters during electrodeposition but also improves distribution of Pt particles.[42]

To further reveal the electrodeposition of the Pt particles, FESEM/EDS spectra were recorded for the composite material. A typical SEM image and selected rectangular area used for EDS studies of Pt deposited on rGO/PEDOT:PSS(EG) are shown in Fig. 3a. The EDS reveals the presence of carbon (from PEDOT and rGO), sulfur (from PEDOT and PSS), oxygen (from PEDOT:PSS, rGO and EG) and Pt nanoparticles. Fig. 3c shows SEM images depicting a heterogeneous morphology for a rGO/PEDOT:PSS(EG)/Pt. The composite reveals globular microstructure characteristic of PEDOT and a wrinkled morphology which is a characteristic feature of rGO. The lighter areas are agglomerated Pt particles homogenously distributed onto the surface as confirmed by EDS data (Fig. 3b). Electrochemically deposited Pt nanoparticles tend to agglomerate instead of dispersed nanoparticles on the surface of the substrate.[9] The elemental mapping images of (Fig. 3d) reveals a homogeneous distribution of C, O and S (Fig. 3d(i–iii)) throughout the composite while some larger aggregated Pt within the mapped area is observed (Fig. 3d(iv)).

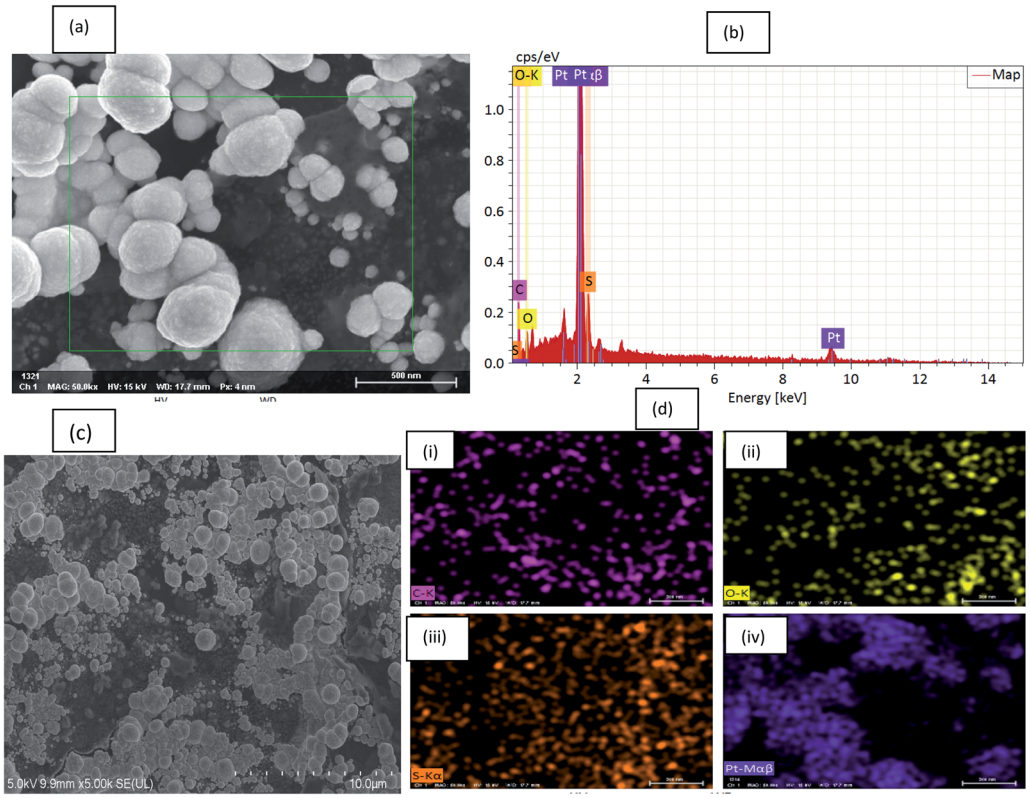

Fig. 3 (a) SEM images of rGO/PEDOT:PSS(EG)/Pt(30%) used for EDS (×50k), (b) EDS spectrum, (c) SEM image of rGO/PEDOT:PSS(EG)/Pt(30%) and (d) elemental color maps for (i) carbon, (ii) oxygen, (iii) sulfur and (iv) platinum.

Electrochemical characterisation

Cyclic voltammetric studies. The cyclic voltammograms for the different Pt loading (10–40%) on PEDOT:PSS and 30% Pt deposited on various rGO/PEDOT:PSS composite electrodes are depicted in Fig. 4a and b, respectively. The figures show the characteristics hydrogen adsorption–desorption peaks between 0.05 V and 0.3 V, a double layer region up to 0.55 V and Pt oxide formation and reduction at a higher potential between 0.6–0.95 V *vs.* RHE except for 10% loading (Fig. 4a). The exception in the cyclic voltammogram of 10% Pt on PEDOT:PSS is because the electrochemistry of the polymer support dominates the electrochemical behaviour which hides the Pt finger print.[43] ECSA for PEDOT:PSS/Pt(30%) is higher than PEDOT:PSS/Pt(40%) in the presence and absence of EG. This indicates that Pt particles tend to form progressively larger agglomerates up on increase in Pt loading. In an ideal case in which the particle size is constant and no agglomerates are formed, the ECSA should be constant for different loadings.[44]

The oxide reduction peak in Fig. 4b increase when PEDOT:PSS(EG) was added to rGO until the w/w ratio is 1 : 3 and reduced on further addition of PEDOT:PSS (1 : 5). The reduction peak

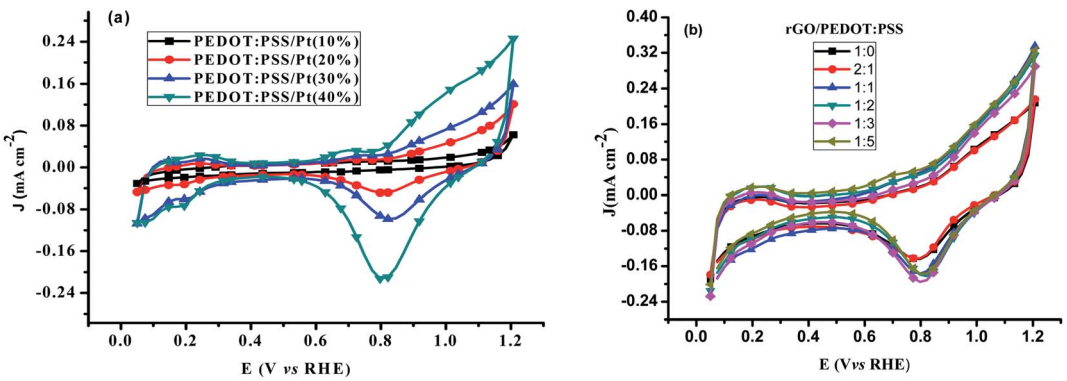

Fig. 4 Cyclic voltammograms of (a) different wt% Pt catalyst on PEDOT:PSS (b) rGO:PEDOT:PSS(EG)/Pt(30%) catalyst in N_2 saturated 0.1 M $HClO_4$ at scan rate of 20 mV s^{-1}.

potential is also shifted to more positive value with a maximum shift of about 30 mV for 1 : 2 ratio. The real surface area (A_r) of platinum determined by charge integration under the hydrogen adsorption peaks increased from 0.5 cm^2 to 0.8 cm^2 as the amount of rGO/PEDOT:PSS ratio increased from 1 : 0 to 1 : 5.

Linear sweep voltammetric studies at RDE. The ORR activity was further investigated using linear sweep voltammetric method at a RDE. The polarization curves of the ORR at PEDOT:PSS/Pt modified GC electrode for different Pt loadings are shown in Fig. 5a. These polarisation curves show the characteristics diffusion-controlled region (<0.6 V), mixed diffusion kinetic limitation region (0.6–0.8 V) and Tafel region (>0.8 V).[34] As expected, more positive onset potential and higher limiting current density were obtained for the highest Pt loading (PEDOT:PSS/Pt) (40%). The electrocatalytic ORR activity of was studied by adding EG to PEDOT:PSS ink. PEDOT:PSS(EG) modified GC electrode was also used in the comparison as a reference. The onset potential and the current density are remarkably improved after platinum is deposited on PEDOT:PSS(EG). The limiting current density for ORR on PEDOT:PSS/Pt is increased upon addition of EG onto PEDOT:PSS ink (Fig. 5b). The increase in the limiting current upon addition EG shows that the presence of EG promotes Pt particle coverage and distribution. Moreover, 30% and 16% increase in ECSA for 30% and 40% Pt loading, respectively, was observed for PEDOT:PSS(EG), showing that the increase in ECSA was more pronounced at the lower Pt loading (30%). Therefore, EG enhances the dispersion of Pt particle with large area coverage and hence increases Pt utilisation.[28,44] The kinetic currents (i_k) extracted from Fig. 5b were used to calculate mass activity (MA) and the specific activity (SA) of the electrocatalyst using eqn (4) and (5). The calculated values are summarised in Table S1.† An increase in SA of 1.2 and 1.1 fold and a 1.5 and 1.2 fold increase in MA were obtained at 0.81 V by the addition of EG on PEDOT:PSS for 30% and 40% Pt loading, respectively. These enhancements were attributed to a change in platinum morphology and inhibition of agglomeration of Pt nanoparticles during the process of electrodeposition by the addition of EG.[28,44]

Hence, using this pronounced effect of EG at 30% Pt loading different ratio of rGO and PEDOT:PSS(EG) were further investigated. Typical background-corrected polarisation curves for the rGO and rGO/PEDOT:PSS(EG) composite supported catalyst in 0.1 M $HClO_4$ at 1600 rpm are shown in Fig. 5c. More positive onset potentials and higher limiting current densities were obtained as the percentage of PEDOT:PSS increased from 1 : 0 to 1 : 2. Increasing the percentage of PEDOT:PSS beyond 1 : 2 to 1 : 3 and 1 : 5 lowers the onset potential and limiting current density. Hence, rGO/PEDOT:PSS(EG) (1 : 2)/Pt 30% which gave a 2.2 and 2.9 fold increase in the SA and MA at 0.81 V, respectively, was found to be the optimum composition. rGO modified GC electrode (Fig. 5C) shows a clear reduction pre-wave at low overpotential, followed by a second reduction wave starting at around −0.013 V, which is indicative of a prevalent 2e reduction pathway.[30] The onset potential and the current density are remarkably improved after platinum is deposited on rGO.

The mass transport corrected Tafel plots ($\log|j_k|$ *vs.* E) for PEDOT:PSS/Pt, PEDOT:PSS(EG)/Pt, and rGO/PEDOT:PSS(EG)/Pt are shown in Fig. 6. The figures show a transition in the Tafel slope from 60 mV per decade to 120 mV per decade for all the catalysts. The observed Tafel slope of ~60 mV per decade at low overpotentials is associated to an oxygen reduction process on an oxide-covered Pt, and the 120 mV per decade slope at higher

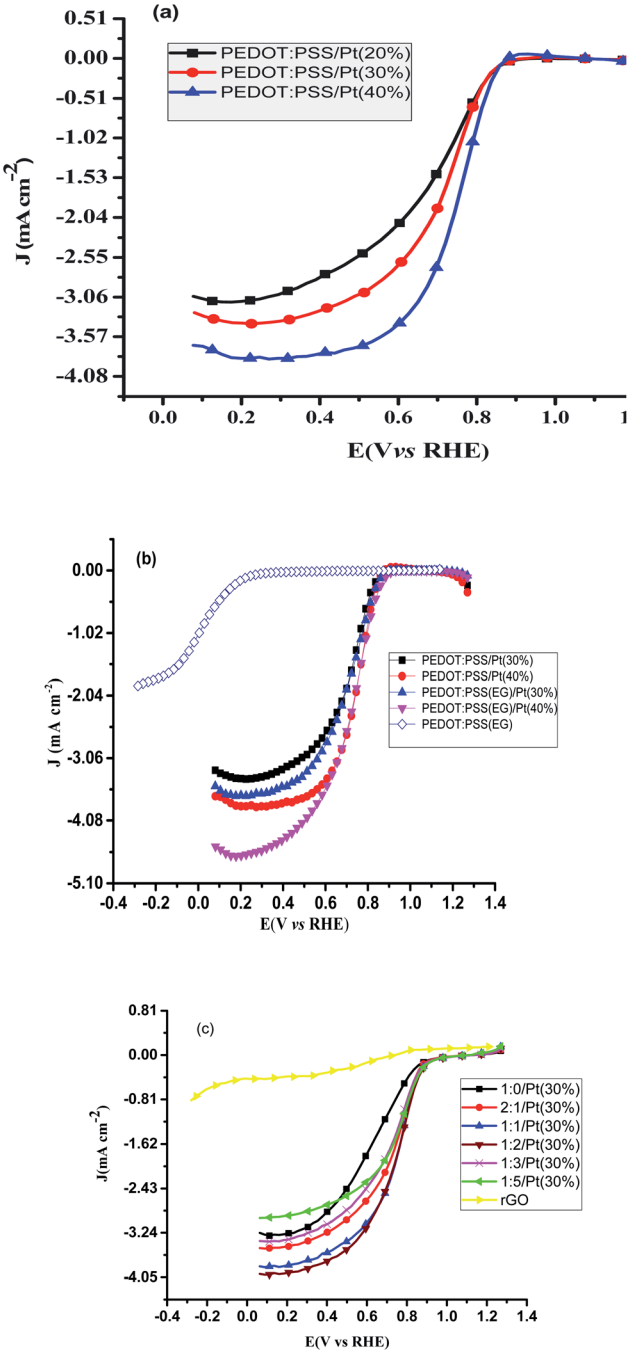

Fig. 5 Background corrected oxygen polarization curves for (a) PEDOT:PSS/Pt, (b) PEDOT:PSS(EG), 30% and 40% platinum on PEDOT:PSS(EG) and PEDOT:PSS (c) rGO and rGO/PEDOT:PSS/Pt(30%) in O_2-saturated 0.1 M $HClO_4$ at a scan rate of 20 mV s^{-1} rotating at 1600 rpm.

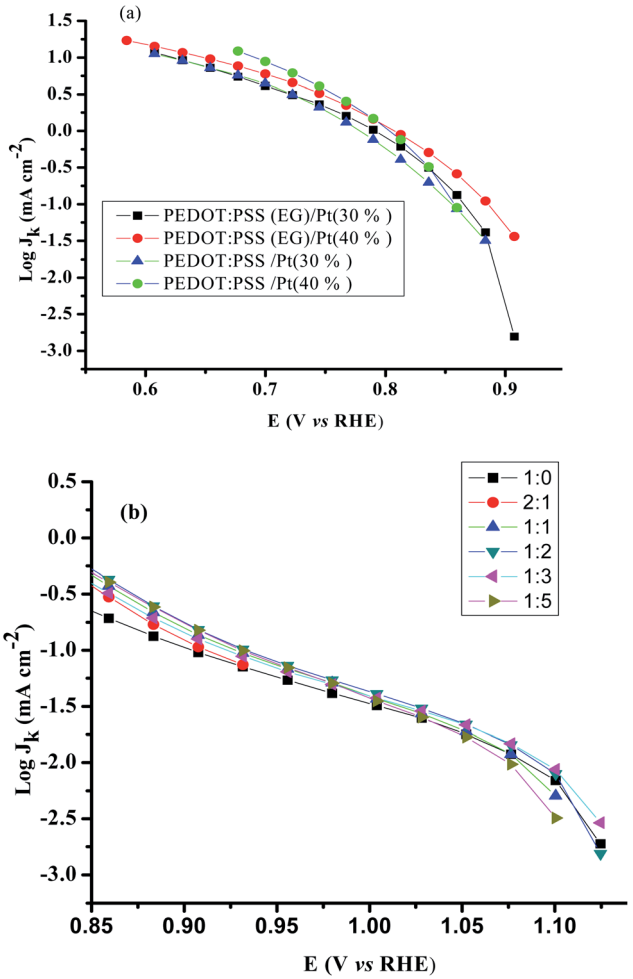

Fig. 6 Mass transport corrected Tafel plots for (a) PEDOT:PSS/Pt, PEDOT:PSS(EG)/Pt and. (b) rGO/PEDOT:PSS(EG)/Pt obtained from disk current in the cathodic sweep at 1600 rpm. Scan rate: 20 mV s^{-1}.

overpotentials is related to reduction process taking place on oxide-free Pt surfaces.[45] The addition of EG reduces the Tafel slope for both the 30 and 40% Pt loading (Table 1) which confirms more favourable kinetics for ORR.[46]

Linear sweep voltammetric studies at RRDE. RRDE measurements are used to assess the extent of peroxide formation, the number of electrons transferred per O_2 molecule (n), and the ORR pathway. The disk current represents the oxygen reduction current referring to the ORR activity. The ring current indicates the oxidation current of intermediates on the Pt ring electrode, referring to the production of H_2O_2 during the ORR process. The most positive onset potential and largest limiting current density on the disk electrode as well as very low ring currents characterises the perfect catalytic material for the 4-electron ORR. Fig. 7a and b shows typical RRDE voltammograms including the ring and the disk currents *vs.* the disk potential for rGO/PEDOT:PSS(EG)/Pt at different rGO and PEDOT:PSS ratios. The number of electrons transferred (n) derived from RRDE result using eqn (6) over the potential range of 0.07 to 0.3 V were 3.86, 3.88, 3.92, 3.93, 3.91, and 3.85, respectively for 1 : 0, 2 : 1, 1 : 1, 1 : 2, 1 : 3 and 1 : 5 as shown in Fig. 7c which confirms the improvement of the electrocatalytic activity of rGO up on the addition of PEDOT:PSS(EG). The percentage of H_2O_2 generated was quantified using eqn (7) and found to be 7.9% for 1 : 0 composition and significantly reduced to 3.3% for 1 : 2 composition (Fig. 7d). Hence, the 1 : 2 composition (rGO/PEDOT:PSS(EG)/Pt) exhibits the largest limiting current density (on the disk electrode), the most positive onset potential, and the lowest % H_2O_2 indicating an excellent ORR activity *via* the 4-electron pathway. The detection of hydrogen peroxide at potentials below 0.8 V in Fig. 7b indicates that the two-electron pathway does in fact occur on the surface of rGO/PEDOT:PSS(EG)/Pt(30%). The yield of H_2O_2 increase with decreasing potential and a significant increase in H_2O_2 formation was observed at potentials <0.1 V. This can partly be attributed to the blockage of surface active sites by adsorbed hydrogen atoms, preventing the dissociative adsorption of oxygen molecules.[47] The higher activity and number of electron transfer observed for rGO/PEDOT:PSS(EG) (1 : 2)/Pt(30%) could be related to the decreased H_2O_2 formation by further reduction of H_2O_2 to H_2O.[44] Therefore, the electrocatalytic ORR on rGO/PEDOT:PSS(EG)/Pt(30%)largely proceeds *via* a sequential pathway *via* H_2O_2 species, rather than *via* direct reduction of O_2.

Table 1 Comparison of the kinetic parameters of electrocatalyst materials for ORR with literature values[a]

Samples	Pt loading (μg cm^{-2})	A_r (cm^2)	ECSA (m^2 g^{-1})	Tafel slope (mV dec^{-1}) lcd/hcd	n	SA (μA cm$_{Pt}^{-2}$)	MA (mA mg$_{Pt}^{-1}$) 0.8 V	Reference
Pt/C (pulse current deposition), (EG)	55	1.83	16.9	—	—	33[c]	5.6[c]	28
PEDOT:PSS/Pt	73	0.8	15.5	66/159	—	17[b]	—	43
PEDOT:PSS/Pt	138	1.5	15.37	90/200	3.7	87[b]	—	43
PEDOT:PSS/Pt(30%)	71	0.41	2.93	68/154	3.46	132[d], 156[e]	4.62[e]	This work
PEDOT:PSS/Pt(40%)	110	0.526	2.32	70/133	3.71	137[d], 291[e]	7.1[e]	This work
PEDOT:PSS(EG)/Pt(30%)	71	0.526	3.8	61/146	3.75	144[d], 175[e]	6.65[e]	This work
PEDOT:PSS(EG)/Pt(40%)	110	0.61	2.68	62/120	3.91	262[d], 376[e]	10.61[e]	This work
rGO/PEDOT:PSS(EG) (1 : 2)/Pt(30%)	71	0.65	4.72	66/125	3.93	158[d], 188[e]	10.54[e]	This work

[a] Lcd/hcd – low current density/high current density. [b] Rotational rate = 750 rpm, E (V *vs.* RHE) = 0.836. [c] Rotational rate = 1000 rpm, E (V *vs.* RHE) = 0.8. [d] Rotational rate = 400 rpm, E (V *vs.* RHE) = 0.836. [e] Rotational rate = 900 rpm, E (V *vs.* RHE) = 0.836.

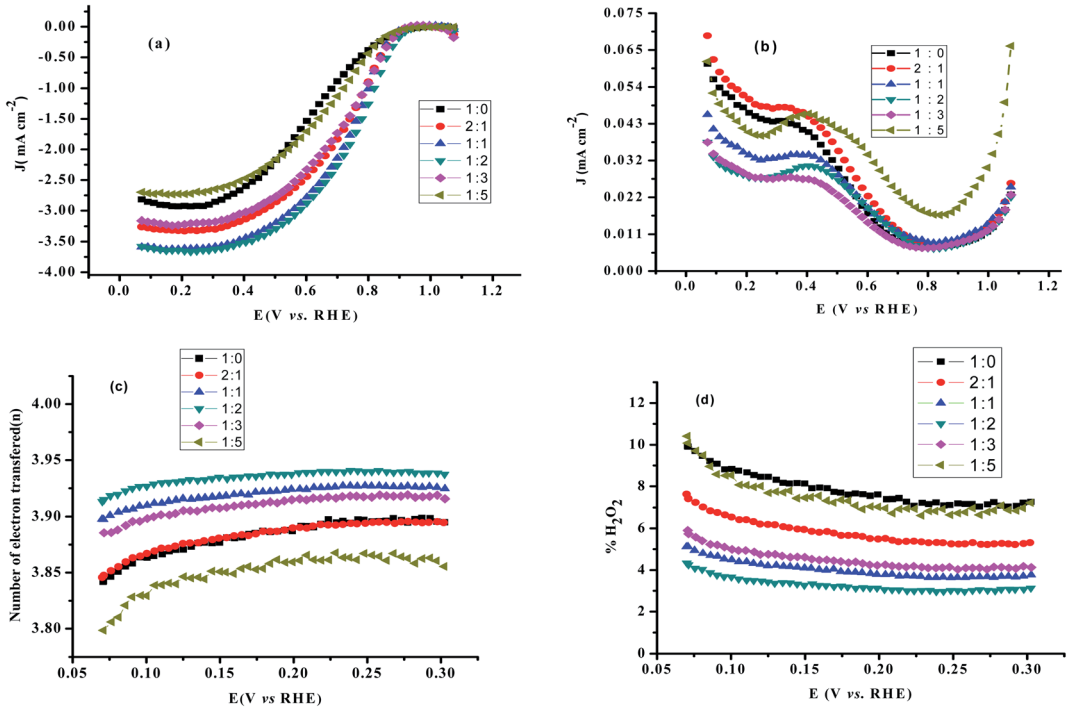

Fig. 7 (a) RRDE voltammograms disk current density (b) ring current density, (c) the number of electron transferred, and (d) % H_2O_2 formation as a function of the disk potential for various rGO/PEDOT:PSS composite at 1600 rpm in 0.1 M $HClO_4$ solution.

For comparison, the RRDE voltammograms, n, and % H_2O_2 formation as a function of the disk potential for various Pt loadings (10%, 20%, 30% and 40%) on PEDOT:PSS(EG) were studied and are shown in Fig. S3.† The % H_2O_2 yield determined for 10%, 20%, 30% and 40% Pt loading on PEDOT:PSS(EG) were found to be 52%, 24%, 12%, and 4.5%, respectively. The electron transfer numbers (n) over the potential range of 0.07 to 0.3 V were found to be 2.96, 3.52, 3.78, and 3.91, respectively, for 10, 20, 30, and 40% Pt loading on PEDOT:PSS(EG). PEDOT:PSS(EG)/Pt(10%) displays the largest % H_2O_2 indicating that the electrochemistry is largely dominated by the PEDOT:PSS.[43] The % H_2O_2 yields and n for 30% Pt loading on PEDOT:PSS(EG), rGO and rGO/PEDOT:PSS(EG) (1 : 2) are shown in Fig. 8. Lower % H_2O_2 and higher n were found for Pt particles deposited on rGO/PEDOT:PSS(EG) composite. The MA for ORR on Pt particles deposited on rGO, PEDOT:PSS(EG) and rGO/PEDOT:PSS(EG) were found to be 7.8, 8.7, and 22.3 A g^{-1}, respectively (Table S1†). Hence, a 2.9 fold increase in mass activity was found in the optimised composite ratio.

The electrocatalytic performance of the optimized composite material was compared with previously reported values of Pt deposited on PEDOT:PSS and Vulcan carbon treated with EG (Table 1). The composite show better electrocatalytic performance and the use of commercially available materials (PEDOT:PSS and rGO) and their synergistic effect further gives promise for wide spread application.

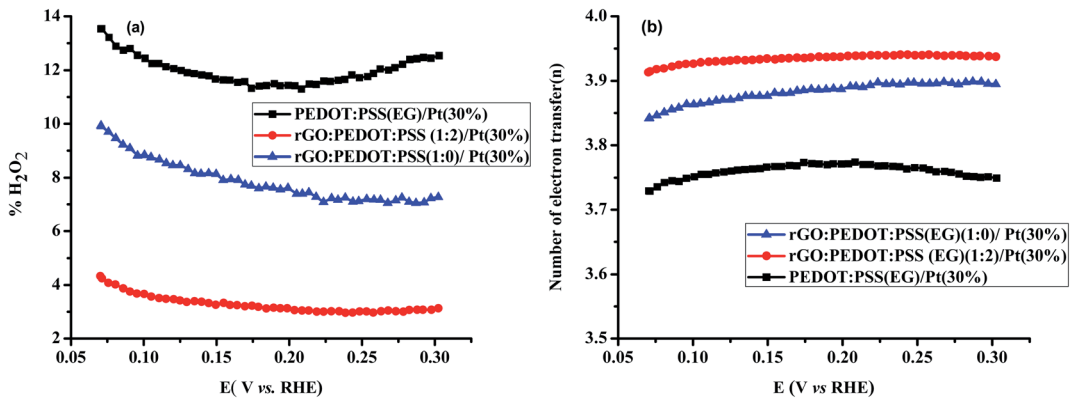

Fig. 8 (a) % H_2O_2 and (b) n as a function of the disk potential for PEDOT:PSS(EG)/Pt(30%), rGO/PEDOT:PSS(EG) (1 : 0)/Pt(30%) and rGO/PEDOT:PSS(EG) (1 : 2)/Pt(30%) at 1600 rpm in 0.1 M $HClO_4$ solution.

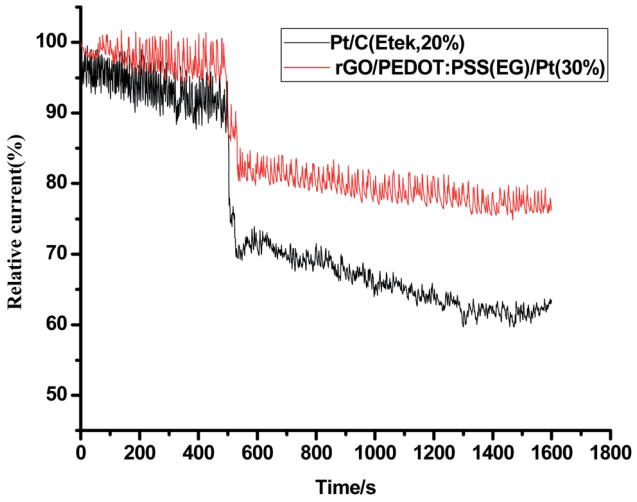

Fig. 9 Comparative study of methanol tolerance ability of rGO/PEDOT:PSS(EG)/Pt(30%) and Pt/C (Etek, 20%) by chronoamperometry at 0.8 V in O_2-saturated 0.1 $MHClO_4$ with a rotational speed of 1600 rpm.

Stability and electrochemical crossover effect are two important factors to evaluate the performance of an electrocatalyst in fuel cells. To further verify the electrocatalytic performance of the catalyst, a small quantity of 3 M methanol was introduced at 500th s in chronoamperometric (CA) measurement (Fig. 9) for ORR at rGO/PEDOT:PSS(EG)/Pt(30%) and commercial Pt/C (Etek, 20%). A sharp and immediate jumping in current on rGO/PEDOT:PSS(EG)/Pt(30%) and commercial Pt/C catalyst upon the addition of methanol indicates the occurrence of methanol oxidation. The rGO/PEDOT:PSS(EG)/Pt(30%) electrode exhibited better methanol tolerance with 15% current decay compared with a 22% current decay for commercial Pt/C electrode. The durability of rGO/PEDOT:PSS(EG)/Pt(30%) and commercial Pt/C catalysts was also investigated by *I–t* measurement. As shown in Fig. 10, rGO/PEDOT:PSS(EG)/Pt(30%) exhibits a very slow attenuation with high current retention 96.02% after 9000 s. By contrast, the Pt/C electrode exhibited a gradual decrease with 86.2% current retention after the same period indicating that rGO/PEDOT:PSS(EG)/Pt(30%) electrocatalyst is much more stable than the commercial Pt/C catalyst.

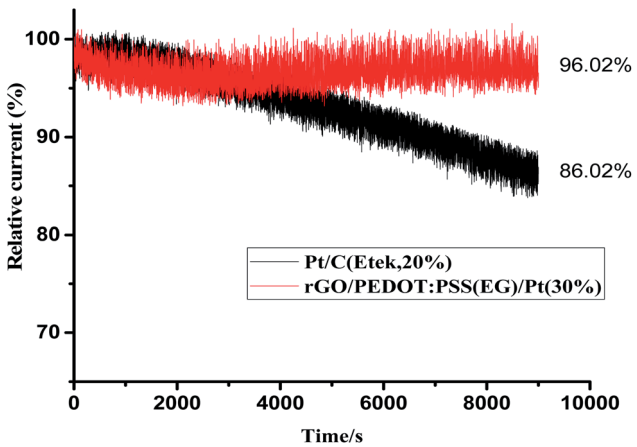

Fig. 10 Chronoamperometric responses of rGO/PEDOT:PSS(EG)/Pt(30%) and Pt/C (Etek, 20%) by chronoamperometry at 0.8 V in O_2-saturated 0.1 $MHClO_4$ with a rotational speed of 1600 rpm.

Conclusions

Electrodeposited Pt on rGO, PEDOT:PSS, PEDOT:PSS(EG) and rGO/PEDOT:PSS(EG) were demonstrated for electrocatalytic reduction of oxygen in acidic solution. Reduced particle size and higher dispersion of Pt nanoparticle are responsible for the improved catalytic activity of PEDOT:PSS up on the addition of EG. Analysis of the electrochemical reduction of oxygen at rGO/PEDOT:PSS(EG) (1 : 2)/Pt(30%) reveals enhanced catalytic activity with highest limiting current, lowest onset potential, maximum SA and MA with lowest H_2O_2 yield towards oxygen reduction reaction in acidic solution compared to PEDOT:PSS, PEDOT:PSS(EG) and rGO. rGO/PEDOT:PSS(EG)/Pt(30%) exhibits better tolerance to methanol crossover effect and longer durability than that of the Pt/C catalyst. The composite of rGO and PEDOT:PSS(EG) is a promising support material for platinum in the oxygen reduction reaction.

Conflicts of interest

There are no conflicts to declare.

Acknowledgements

Financial support from the Basic and Applied Basic Research Major Program of Guangdong Province (No. 2019B030302007), the Institute of Polymer Optoelectronic Materials and Devices, School of Materials Science and Engineering, South China University of Technology, Guangzhou, PR China and International Science Program, Uppsala University, Sweden, is acknowledged.

Notes and references

1 K. Jukk, N. Kongi, A. Tarre, A. Rosental, A. B. Treshchalov, J. Kozlova, P. Ritslaid, L. Matisen, V. Sammelselg and K. Tammeveski, *J. Electroanal. Chem.*, 2014, **735**, 68–76.
2 N. Zhang, L. Lingcong, Y. Chu, L. Zheng, S. Sun, G. Zhang, H. He and J. Zhaob, *Catal. Today*, 2019, **332**, 101–108.
3 X. Song, N. Li, H. Zhang, H. Wang, L. Wang and Z. Bian, *J. Power Sources*, 2019, **435**, 226771.
4 M. K. L. Mendoza, B. J. V. Tongol, S. Shanmugam and H. Kim, *Int. J. Hydrogen Energy*, 2018, **43**, 19930–19938.
5 Q. Liu, S. Cao and Y. Qiu, *Int. J. Hydrogen Energy*, 2017, **42**, 29274–29282.
6 A. Jindal, D. K. Gautam and S. Basu, *J. Electroanal. Chem.*, 2016, **775**, 198–204.
7 F. Jiang, Z. Yao, R. Yue, J. Xu, Y. Du, P. Yang and C. Wang, *J. Solid State Electrochem.*, 2013, **17**, 1039–1047.
8 C. Coutanceau, M. J. Croissant, T. Napporn and C. Lamy, *Electrochim. Acta*, 2000, **46**, 579–588.

9 S. Patra and N. Munichandraiah, *Langmuir*, 2009, **25**, 1732–1738.
10 X. Zhou, J. Qiao, L. Yang and J. Zhang, *Adv. Energy Mater.*, 2014, **4**, 1301523.
11 D. Higgins, P. Zamani, A. Yu and Z. Chen, *Energy Environ. Sci.*, 2016, **9**, 357–390.
12 H. Feng, Y. Liu and J. Li, *Chem. Commun.*, 2015, **51**, 2418–2420.
13 M. B. Gastelum, M. I. S. Gastelum, J. R. F. Hernandez, G. G. Botte, S. P. Sicairos, T. R. Castanon, E. R. Soto and R. M. F. Navarro, *Energy*, 2019, **181**, 1225–1234.
14 Y. Li, Y. Li, E. Zhu, T. McLouth, C. Y. Chiu, X. Huang and Y. Huang, *J. Am. Chem. Soc.*, 2012, **134**, 12326–12329.
15 G. G. Kumar, C. J. Kirubaharan, S. Udhayakumar, C. Karthikeyan and K. S. Nahm, *Ind. Eng. Chem. Res.*, 2014, **53**, 16883–16893.
16 E. Antolini and E. R. Gonzalez, *Appl. Catal., A*, 2009, **365**, 1–19.
17 T. Getachew, F. Addis, T. Beyene, S. Mehretie and S. Admassie, *Bull. Chem. Soc. Ethiop.*, 2019, **33**, 359–372.
18 S. D. Domínguez, J. A. Pardilla, A. B. Murcia, E. Morallon and D. C. Amoros, *J. Appl. Electrochem.*, 2007, **38**, 259.
19 K. Sun, S. Zhang, P. Li, Y. Xia, X. Zhang, D. Du, F. H. Isikgor and J. Ouyang, *J. Mater. Sci.: Mater. Electron.*, 2015, **26**, 4438–4462.
20 T. Cheng, Y. Z. Zhang, J. D. Zhang, W. Y. Lai and W. Huang, *J. Mater. Chem. A*, 2016, **4**, 10493–10499.
21 Y. Xia, K. Sun and J. Ouyang, *Adv. Mater.*, 2012, **24**, 2436–2440.
22 B. W. Jensen, O. W. Jensen, M. Forsyth and D. R. MacFarlane, *Science*, 2008, **321**, 671–674.
23 B. Wondimu and S. Admassie, *Bull. Chem. Soc. Ethiop.*, 2012, **26**, 449–454.
24 M. Zhang, W. Yuan, B. Yao, C. Li and G. Shi, *ACS Appl. Mater. Interfaces*, 2014, **6**, 3587–3593.
25 Y. Nie, L. Li and Z. Wei, *Chem. Soc. Rev.*, 2015, **44**, 2168–2201.
26 C. Che, M. Vagin, K. Wijeratne, D. Zhao, M. Warczak, M. P. Jonsson and X. Crispin, *Adv. Sustainable Syst.*, 2018, **2**, 1800021.
27 H. Shi, C. Liu, Q. Jiang and J. Xu, *Adv. Electron. Mater.*, 2015, **1**, 1500017.
28 W. Yohannes, S. V. Belenov, V. E. Guterman, L. M. Skibina, V. A. Volotchaev and N. V. Lyanguzov, *J. Appl. Electrochem.*, 2015, **45**, 623–633.
29 F. Chekol, S. Mehretie, F. Addis, T. Tolcha, N. Megersa and S. Admassie, *Electroanalysis*, 2019, **31**, 1104–1111.
30 S. K. Bikkarolla, P. Cumpson, P. Joseph and P. Papakonstantinou, *Faraday Discuss.*, 2014, **173**, 415–428.
31 B. W. Zewde and S. Admassie, *J. Power Sources*, 2012, **216**, 502–507.
32 L. F. Gloaguen, J. M. Leager and C. Lamy, *J. Appl. Electrochem.*, 1997, **27**, 1052–1060.
33 J. Schmidt, H. A. Gasteiger, G. D. Stab, P. M. Urban, D. M. Kolb and R. J. Behm, *J. Electrochem. Soc.*, 1998, **145**, 2354–2358.
34 Q. He and S. Mukerjee, *Electrochim. Acta*, 2010, **55**, 1709–1719.
35 X. Min, Y. Chen and M. W. Kanan, *Phys. Chem. Chem. Phys.*, 2014, **16**, 13601–13604.
36 Y. Garsany, O. A. Baturina, E. S. Lyons and S. S. Kocha, *Anal. Chem.*, 2010, **82**, 6321–6328.
37 Y. Saito and T. Kikuchi, *Voltammetry Theory, Types and Application*, Nova Science Publishers, Inc., New York, 2014.
38 W. J. Khudhayer, N. N. Kariuki, X. Wang, D. J. Myers, A. U. Shaikh and T. Karabacak, *J. Electrochem. Soc.*, 2011, **158**, B1029–B1041.
39 M. E. Scofield, H. Liu and S. S. Wong, *Chem. Soc. Rev.*, 2015, **44**, 5836–5860.
40 G. Zhang, Q. Wei, X. Yang, A. C. Tavares and S. Sun, *Appl. Catal., B*, 2017, **206**, 115–126.
41 Y. Chen, X. Zhu, D. Yang, P. Wangyang, B. Zeng and H. Sun, *Electrochim. Acta*, 2019, **298**, 297–304.
42 Y. Wang, N. Zhao, B. Fang, H. Li, X. T. Bi and H. Wang, *RSC Adv.*, 2015, **5**, 56570–56577.
43 J. Shan and P. G. Pickup, *Electrochim. Acta*, 2000, **46**, 119–125.
44 E. Fabbri, S. Taylor, A. Rabis, P. Levecque, O. Conrad, R. Kotz and T. J. Schmidt, *ChemCatChem*, 2014, **6**, 1410–1418.
45 E. T. Salgado, D. B. Uribe, P. A. M. Aguilar, J. L. R. Rodriguez, R. C. Silva and O. S. Feria, *Electrochim. Acta*, 2019, **298**, 172–185.
46 S. Chen, J. Duan, J. Ran, M. Jaroniec and S. Z. Qiao, *Energy Environ. Sci.*, 2013, **6**, 3693–3699.
47 S. Taylor, E. Fabbri, P. Levecque, T. J. Schmidt and O. Conrad, *Electrocatalysis*, 2016, **7**, 287–296.